LaSen: Low-Altitude Drone Sensing with 5G-NR Signals

Qian Yang[1,2], Yongtao Dai[3], Mingrui Li[3], Qianyi Huang[3], Xu Chen[3], Jin Zhang[1], Guochao Song[4],
Qian Zhang[5], Xiaofeng Tao[6,2]
[1]Southern University of Science and Technology, [2]Peng Cheng Laboratory, [3]Sun Yat-sen University, [4]China Academy of Information and Communications Technology, [5]Hong Kong University of Science and Technology, [6]Beijing University of Posts and Telecommunications.
Email: yangq2022@mail.sustech.edu.cn, {daiyt9, limr36}@mail2.sysu.edu.cn, {huangqy89, chenxu35}@mail.sysu.edu.cn,
zhangj4@sustech.edu.cn, songguochao@caict.ac.cn, qianzh@ust.hk, taoxf@bupt.edu.cn.

Abstract

The surge in low-altitude economic activities has spurred a significant interest in sensing Unmanned Aerial Vehicles (UAVs). With the widespread deployment of 5G infrastructure and the increasing prominence of integrated sensing and communication, monitoring UAVs via 5G base stations is a natural consideration. However, the rapid Doppler shifts of UAVs and sparse 5G reference signals violate Nyquist sampling requirements. To bridge this gap, we propose *LaSen*, which merges reference and downlink data signals for sensing. A key challenge stems from the fact that the combination of the periodic reference signals and stochastic data signals constitutes a non-uniform, time-varying measurement matrix. *LaSen* formulates the tracking of UAVs as a sparse recovery problem, where the target's kinematics are reconstructed from non-uniform, sub-Nyquist observations. *LaSen* overcomes the challenges of volatile 5G signal patterns in an iterative way, starting from good measurements as an anchor and progressively refining the suboptimal measurements. Real-world experiments show that *LaSen* significantly extends the velocity sensing capability, where the measurable speed is up to 20.2 m/s. *LaSen* can detect drones at a distance of 108 m and can continuously track the distance and velocity of multiple targets, even when the downlink channel is sparsely and dynamically occupied. This work demonstrates the feasibility of high-speed target sensing in next-generation dual-function 5G/6G infrastructures.

CCS Concepts

• **Hardware → Sensor applications and deployments**; **Wireless devices**.

Keywords

Integrated Sensing and Communication, UAV Sensing, 5G New Radio, Compressive Sensing, Range-Doppler Recovery.

ACM Reference Format:
Qian Yang, Yongtao Dai, Mingrui Li, Qianyi Huang, Xu Chen, Jin Zhang, Guochao Song, Qian Zhang, Xiaofeng Tao. 2026. *LaSen*: Low-Altitude Drone Sensing with 5G-NR Signals. In *ACM/IEEE International Conference on Embedded Artificial Intelligence and Sensing Systems (SenSys '26), May 11–14, 2026, Saint Malo, France.* ACM, New York, NY, USA, 14 pages. https://doi.org/10.1145/3774906.3800504

SenSys '26, Saint Malo, France

ACM ISBN 979-8-4007-2309-4/26/05
https://doi.org/10.1145/3774906.3800504

1 Introduction

The low-altitude economy is rapidly gaining momentum worldwide, fueled by exponential growth in drone delivery services, urban air mobility, and emergency response applications. It is estimated that the global market volume for commercial UAVs could rise from 35 billion US dollars in 2024 to around 58 billion US dollars by 2030 [1]. Monitoring these UAVs is critical not only to ensure airspace safety and prevent collisions, but also to support efficient urban management. Effective tracking enables authorities to manage traffic, enforce regulatory compliance, and address privacy concerns.

While a variety of methods exist for tracking UAVs, including acoustic-based [20, 21, 44], vision-based [14, 36], and radar techniques [23, 27, 42, 52], they typically require specialized deployment and dedicated infrastructure. Given the growing prominence of the integrated sensing and communication (ISAC) paradigm, it is natural to consider monitoring UAVs via widely deployed 5G base stations (gNBs). It eliminates the need for dedicated sensing systems and leverages existing communication infrastructure to enable pervasive sensing. Moreover, the superior penetration capability of RF signals allows them to outperform vision-based methods in adverse weather conditions such as rain and fog.

Similar to radar pulses, gNBs also transmit periodic reference signals for synchronization or downlink channel estimation. Most prior work on 5G New Radio (NR) / 4G Long Term Evolution (LTE)-based sensing relies on customized signals [22, 31] or reference signals [10, 11, 17, 18, 25, 28, 37, 40, 41, 49]. However, for the sake of resource efficiency, 5G NR eliminates mandatory, high-frequency periodic reference signals. The maximum configurable repetition frequency for Sub-6 GHz Channel State Information Reference Signals (CSI-RS) is 500 Hz [3], falling short of the Nyquist sampling requirements for resolving high-speed targets like drones. For example, to detect drones moving at 100 mph with a 3.5 GHz gNB, the Nyquist sampling rate is approximately 2 kHz, which is 4 times the CSI-RS repetition frequency. In addition, since the CSI-RS occupies only a small fraction of the time-frequency grid, its integrated energy is low, which directly limits the sensing range for low-RCS micro-UAVs. This exposes a fundamental conflict in ISAC systems, where communication prioritizes resource efficiency while effective sensing requires dense, redundant frames. To reconcile this conflict, we observe that a monostatic ISAC gNB can exploit all non-empty resource elements for channel measurements, including both reference and data-bearing symbols, thereby complementing the reference signals to mitigate undersampling-induced ambiguity without incurring additional resource consumption.

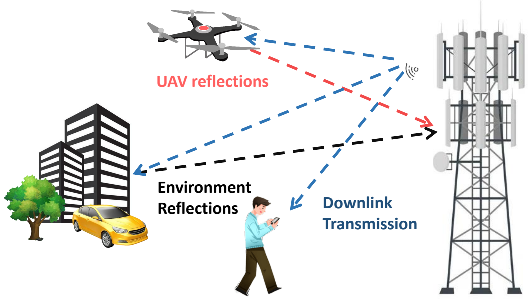

Figure 1: A UAV sensing scenario of *LaSen*.

Although sensing with all transmitted resources sounds promising, the uncertainty of real-time user traffic complicates its practical deployment. Unlike regular reference signals, downlink data signals are stochastic in both the temporal and frequency domains, as their patterns depend on user requests and resource allocation strategies. Therefore, this brings us the following challenges that must be addressed to achieve robust UAV range and velocity estimation:

Two-Dimensional Non-Uniform Sampling. The combination of periodic reference signals and stochastic data signals results in a non-uniform sampling pattern across the time and frequency domain. This irregular structure introduces significant spectral leakage and artifacts during the range-Doppler transformation, degrading the instantaneous estimation accuracy within each sensing frame. The problem is further exacerbated by high-speed UAVs, which cause rapid channel variations that render conventional interpolation ineffective across consecutive missing symbols [37]. Moreover, single-dimensional sparse recovery methods suffer from inconsistent reconstruction performance due to fluctuating bandwidth occupancy across symbols [39]. These reconstruction errors will propagate into both range and velocity estimates, highlighting the need for an approach that can handle the two-dimensional non-uniform sampling.

Time-Varying Resource Availability Across Frames. The dynamic allocation of 5G resources leads to fluctuating bandwidth occupancy between consecutive sensing frames. During peak traffic periods, data transmission utilizes a larger bandwidth, whereas during idle periods, the data occupies only a small fraction of the available bandwidth. Our measurements indicate that sparse occupation of the channel is more prevalent than dense occupation. These frame-to-frame variations cause instability in signal energy and sensing resolution, undermining the consistency required for continuous target tracking and motion analysis.

In this paper, we propose *LaSen*, short for Low-altitude UAV Sensing with 5G-NR signals. Figure 1 illustrates a sensing scenario of *LaSen*. In *LaSen*, during the downlink transmission, the 5G base station is transmitting communication packets to mobile users. The transmitted signals are then reflected by surrounding objects, such as UAVs and buildings. These reflections will be captured by an auxiliary receive chain, and then demodulated to obtain Channel Frequency Response (CFR) measurements (Section 2.2) for target range and velocity estimation.

To tackle the first challenge, *LaSen* formulates the UAV range and velocity estimation as a two-dimensional sparse recovery problem under the compressive sensing framework. Unlike traditional Nyquist-based methods, compressive sensing bypasses the need for uniform sampling grids. It reconstructs the sparse representation of the target's kinematics directly from non-uniform, sub-Nyquist observations. *LaSen* tackles the second challenge with a channel-adaptive hierarchical design. We propose a quantitative scoring metric to identify high-quality measurements, which are likely to yield precise range-Doppler estimates. These estimates serve as anchor points to initialize tracking and stabilize tracking trajectories. For the rest of the measurements, *LaSen* constrains the orthogonal matching pursuit (OMP) search space to a localized vicinity around prior estimates, which can effectively amplify the signal-to-clutter ratio by excluding physically infeasible solutions. This reduced search space allows 2D-OMP to deliver accurate tracking results even when the measurement matrix is sparse or ill-conditioned.

We deploy *LaSen* on a software-defined radio (SDR) platform. To replicate the physical layer parameters of commercial 5G gNBs, we first capture over-the-air traffic traces from multiple gNBs using Wireshark and extract their Radio Resource Control (RRC) configuration messages. Based on the decoded subcarrier spacing and time slot configurations from RRC messages, we program the SDR to emulate the corresponding 5G NR frame structures, ensuring alignment with real-world 5G NR signals. Our contributions are summarized as follows:

- We propose *LaSen*, an integrated sensing and communication system that can work reliably with the 5G signals. *LaSen* performs UAV range-velocity estimation by combining both periodic reference signals and dynamic data signals.
- *LaSen* addresses the non-uniformity and temporal fluctuations of data signal characteristics through a channel-adaptive hierarchical framework that combines global and local estimations. Global estimation leverages high-quality measurement segments to provide robust kinematics, while local estimation ensures robust tracking despite poor channel conditions.
- We implement *LaSen* on a software-defined radio platform and conduct comprehensive evaluations to assess its accuracy and latency. Evaluation results show that, compared with 2D-OMP, *LaSen* can reduce the range and velocity estimation error by 51.84% and 82.84%, respectively.

2 Preliminaries

2.1 Primer on 5G NR Physical Resource

The 5G NR transmission resources are organized through a 10 ms radio frame subdivided into 10 subframes, each containing multiple slots composed of Orthogonal Frequency-Division Multiplexing (OFDM) symbols, as illustrated in Figure 2. The number and duration of slots within each subframe dynamically scale with the selected numerology, determined by the Subcarrier Spacing (SCS). In 5G NR, a SCS of 30 kHz is typically used in the Sub-6 GHz bands, whereas 60 kHz and 120 kHz are common numerologies for mmWave operation. For instance, a 30 kHz SCS configuration yields 0.5 ms slots and 14 OFDM symbols. During each transmission, physical resources are organized into a two-dimensional time-frequency grid, also known as the resource grid. The Resource Element (RE) is the fundamental unit of the resource grid, which occupies one

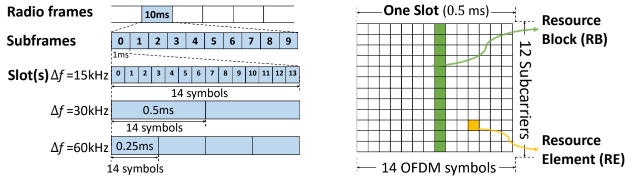

(a) 5G NR data frames (b) 5G NR resource grid

Figure 2: 5G NR Physical Resource.

subcarrier over one OFDM symbol. Twelve consecutive subcarriers form a Resource Block (RB), the minimum schedulable unit.

2.2 Modeling 5G NR Sensing

2.2.1 5G Channel Model. In an OFDM system, wireless transmission in a multipath propagation environment can be represented as the superposition of L distinct propagation paths. Each path is characterized by its complex attenuation α_l, propagation delay τ_l, and Doppler shift $f_{d,l}$. Under this multipath scenario, the CFR $H[m,n]$ at the m-th subcarrier and n-th OFDM symbol can be derived based on the known transmitted reference signal $X[m,n]$ and the received signal $Y[m,n]$ as follows [8]:

$$H[m,n] = \frac{Y[m,n]}{X[m,n]} = \sum_{l=0}^{L-1} \alpha_l e^{-j2\pi(f_0+m\Delta f)\tau_l} e^{j2\pi f_{d,l} n T_{\text{sym}}} + N[m,n], \tag{1}$$

where $f_0, T_{\text{sym}}, N[m,n]$ are carrier frequency (in Hz), OFDM symbol duration (in seconds), and additive noise, respectively. The term $e^{-j2\pi(f_0+m\Delta f)\tau_l}$ indicates the phase shift caused by the propagation delay τ_l, while $e^{j2\pi f_{d,l} n T_{\text{sym}}}$ models the time-varying phase shift introduced by the target Doppler shift. We can find that this model not only characterizes communication channel distortions but also encapsulates sensing-relevant parameters: delays τ_l for ranging and Doppler shifts $f_{d,l}$ for velocity estimation, thus enabling dual-use of 5G NR signals for ISAC.

A practical ISAC implementation involves configuring the gNB with an additional receive chain to capture reflections of its own transmitted signals [32], similar to a monostatic radar. In monostatic configurations, since all of $X[m,n]$ are known, it enables the gNB to achieve channel estimates across all non-empty REs (both reference and data-carrying) within the scheduled bandwidth.

2.2.2 From Channel Frequency Response to Range-Doppler Map. The range–Doppler map of an OFDM channel is obtained with a two-dimensional Fast Fourier Transform (2D-FFT): first, an inverse FFT across the M sub-carriers of the CFR matrix $\mathbf{H} \in \mathbb{C}^{M\times N}$ produces the channel impulse response (CIR), and then an FFT across the N OFDM symbols converts this impulse response into the range–Doppler matrix $\mathbf{Z} \in \mathbb{C}^{M\times N}$; thus $\mathbf{H}$ and $\mathbf{Z}$ form a 2-D Fourier pair, where M counts all active and guard sub-carriers and N is the number of symbols. Through Fourier basis decomposition, the channel frequency response can be expressed as:

$$\mathbf{H} = \mathbf{U}\mathbf{Z}\mathbf{V}^H, \tag{2}$$

where $\mathbf{U} \in \mathbb{C}^{M\times M}$ and $\mathbf{V} \in \mathbb{C}^{N\times N}$ are unitary Fourier basis. $(\cdot)^H$ denotes the Hermitian (conjugate transpose) operator.

3 Motivation and Challenges

3.1 Motivation

3.1.1 Why 5G Reference Signals Fall Short in UAV Sensing? The Federal Aviation Administration (FAA) mandates a maximum permissible speed of 100 mph (44.7 m/s) for UAVs in the United States [16]. In monostatic wireless sensing systems, the Doppler frequency shift (f_d) is proportional to the target velocity (v), governed by the relationship

$$f_d = \frac{2\cdot v}{\lambda}. \tag{3}$$

For a 3.5 GHz carrier, this results in a maximum Doppler shift of 1044 Hz. To avoid aliasing and ensure reliable velocity estimation, the Nyquist-Shannon sampling theorem requires that the measurement signal should be at least twice the frequency of the maximum Doppler shift, i.e., 2087 Hz.

The reference signal architecture in 5G NR fundamentally differs from LTE. LTE utilizes a cell-specific reference signal (CRS) that broadcasts continuously at 1000 Hz, which is widely exploited in existing pervasive sensing studies [11, 17]. While in NR, the design principle is to avoid always-on, mandatory signals such as CRS, reducing spectrum waste and unwanted interference. Thus, NR employs the CSI-RS, a dedicated downlink measurement signal spanning the active bandwidth (e.g., 100 MHz) and serving as a replacement for CRS. To enhance temporal density, the gNB can configure multiple Non-Zero Power (NZP) CSI-RS resource sets with time offsets. As illustrated in Figure 3(a), which shows two sets of periodic CSI-RS with a period of 100 Hz and a 5 ms offset, achieving a maximum sampling rate of 200 Hz.

In addition to CSI-RS, 5G NR incorporates downlink synchronization signals such as the Synchronization Signal Block (SSB), which spans up to 7.2 MHz and is typically repeated at 50 Hz. These relatively low repetition rates (200 Hz for CSI-RS and 50 Hz for SSB) inherently limit Doppler tracking for high-speed targets. To mitigate these constraints, 3GPP introduced the Positioning Reference Signal (PRS) [2], which offers improved time-frequency resolution and higher resource element density through diagonal or staggered RE patterns. However, these benefits come at the cost of increased resource overhead.

3.1.2 Opportunities with Data Signals. Without occupying additional resources, how to mitigate the sensing constraints imposed by sparse reference signals? As we mentioned in Section 2.2, in monostatic configurations, the gNB can obtain channel estimates across all non-empty REs, including both reference and data signals. Figure 3(a) gives a 25 ms channel measurement from a gNB on our campus. We can see that data signals fill the gap between CSI-RS transmissions. Assume that all available REs are occupied by data signals, for a gNB with 30 kHz subcarrier spacing, the average symbol duration is around 0.036 ms, which can measure Doppler frequency up to 14 kHz. By jointly processing these data and reference signals, we can achieve a higher effective sampling rate. It maintains compatibility with standard 5G operation and does not require modifications to existing frame structures or protocols. Furthermore, reusing data signals reduces overhead and avoids the need for additional reference resources, making it a resource-efficient paradigm for ISAC in high-mobility scenarios.

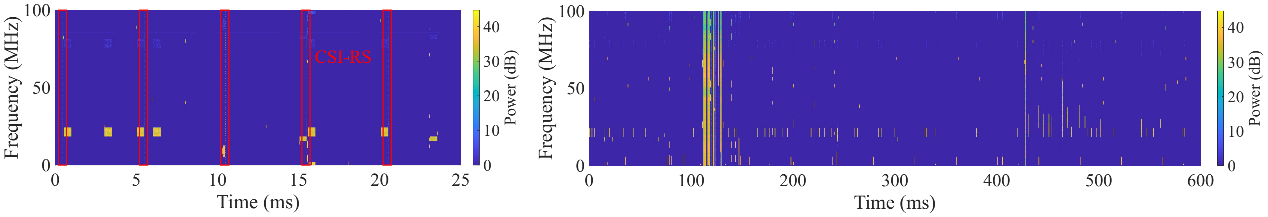

(a) Periodic CSI-RS with intermittent data signals.

(b) 600 ms signal measurement from a gNB.

Figure 3: Measured 5G NR downlink spectrum.

Table 1: Comparison of the UAV target sensing under the dense/sparse downlink channel occupation. The top row represents dense RE occupations, and the bottom row represents sparse RE occupations. The UAV target is highlighted by a bounding box.

Downlink RE Occupations	Ground Truth	*LaSen* (Ours)	2D-OMP	HiSAC	Lerp
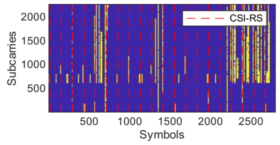	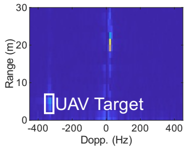	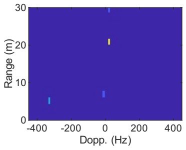	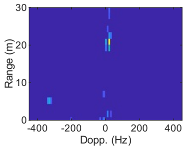	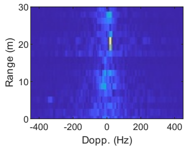	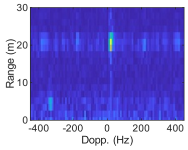
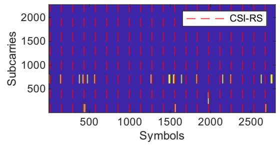	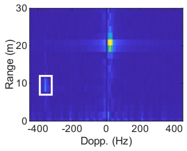	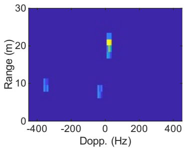	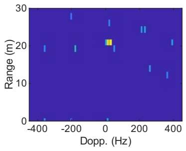	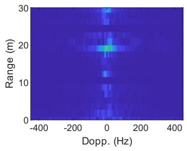	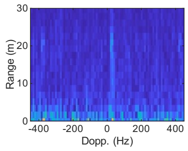

3.2 Design Challenges of *LaSen*

While it sounds straightforward to combine reference signals and data signals for sensing, two main challenges need to be tackled:

Challenge 1: Two-Dimensional Non-Uniform Sampling. To characterize the non-uniformity of real-world resource allocation, we measured the RE occupancy of urban gNBs. Fig. 3(b) depicts signal strength over a 600 ms resource grid, revealing burst-like and clustered RE distributions. This pattern differs significantly from radar systems, which use periodic pulses to maintain uniform sampling and preserve Fourier orthogonality in 2D-FFT.

Table 1 compares different methods under dense and sparse downlink channel conditions over 100 ms. During dense occupation, a UAV target is detected at 5.2 m with a velocity of 10 m/s; after 400 ms (transition to sparse occupation), it moves to 9.5 m with 11 m/s. A common approach to handle non-uniform sampling is interpolation, such as linear interpolation (Lerp) [8], which fills missing channel estimates using adjacent subcarriers or symbols. However, under high UAV mobility, the channel varies rapidly, causing interpolation to fail in the presence of consecutive missing OFDM symbols or subcarriers (the 6th column of Table 1). Single-dimensional compressive sensing methods, such as those leveraging frequency-domain sparsity for range estimation [39], also face challenges. Their performance varies significantly across symbols due to fluctuating signal-to-noise ratio (SNR) and bandwidth (the 5th column of Table 1). These inaccuracies propagate into both range and velocity estimates, underscoring the need for a robust two-dimensional sparse recovery framework.

Challenge 2: Time-Varying Resource Availability Across Frames. The occupancy of the resource grid fluctuates according to the communication demands of the gNB. During periods of high communication traffic, RE occupations are dense (i.e., the first row of Table 1), whereas sparse RE occupancy occurs under low-traffic scenarios (i.e., the second row of Table 1). According to our measurement (Section 4.2.1), dense resource allocation segments constitute just 5% of the total time span, while sparse segments dominate. This time-varying resource availability results in a different sampling structure. Compared with the two rows of Table 1, the bandwidth fluctuations change the signal's energy and range resolution from frame to frame, resulting in detection gaps and lowering overall sensing accuracy.

Although compressive sensing can handle under-sampled scenarios, its performance under sparse occupancy and low SNR remains challenging. In such cases, strong ground clutter often dominates the measurements, causing 2D-OMP and other similar greedy algorithms to recover these prominent components with high priority while overlooking weaker UAV paths. Simply increasing the sparsity level does not resolve the issue, as it tends to overfit noise and introduce false alarms. As shown in the second row of Table 1, all baseline methods fail to detect the UAV accurately under sparse resource conditions. While dense segments provide reliable estimates, relying solely on them results in discontinuous range-Doppler outputs, which severely limit tracking performance for dynamic UAVs.

4 Design of *LaSen*

In this section, we present the design details of *LaSen*. We start with the problem formulation, where we model the UAV tracking problem within a compressive sensing framework, formalizing it as a sparse signal recovery task under non-uniform 5G signals. Next, we address the unique challenges posed by 5G's non-stationary resource allocation patterns.

4.1 Sensing with Non-Uniform Signals

4.1.1 Static Background Suppression. To estimate the velocity and distance of moving UAV targets, the strong static background reflections must first be suppressed. The CFR in Eq. (1) can be decomposed into a *static component* (time-invariant paths when $f_{d,l} = 0$) and a *dynamic component* (time-varying paths when $f_{d,l} \neq 0$), depending on the Doppler frequency shift $f_{d,l}$ of each propagation path l.

To separate static and dynamic channel components, we derive the static component by averaging the CFR over a sufficiently long time interval. During this interval, multipath contributions from the moving UAV undergo phase shifts exceeding 2π, causing their interference effects to average out over time. In contrast, static reflections (e.g., from stationary objects) remain stable. For each subcarrier, we compute the static component as the arithmetic mean of all occupied REs within the interval. Figure 4 shows a comparison of range-velocity maps before and after static-background removal within a 100 ms window. The mean subtraction effectively suppresses strong static background reflections (0 Hz components). However, residual low-speed clutter caused by slow environmental dynamics (e.g., tree leaves) and transceiver self-leakage remains. In Section 4.2.2, we further mitigate the influence of strong energy in these regions using atom isolation.

4.1.2 Range-Doppler Reconstruction. After the static background suppression, there are $K << M \times N$ (K is unknown) dominant dynamic paths' components that remain in CFR with complex gain $\{\alpha_k\}_{k=1}^{K}$. By discretizing Time–frequency plane into an $M \times N$ range-Doppler grid $\mathbf{Z}$, the complex gain on path-k is approximately expressed as the complex gain $z_{m,n}$ on the (m, n)-th grid, or re-indexing as K non-zero values $\{z_k\}_{k=1}^{K}$, corresponding to the path-k's range and Doppler shift.

To reconstruct K-target range-Doppler profile, our goal is to identify the complex coefficient $\{z_k\}_{k=1}^{K}$, where a larger z_k implies that a strong component exists in the corresponding range-Doppler grid. We formulate this reconstruction as a K-sparse compressive sensing problem, especially with the *occupancy characteristic* of the NR downlink transmission. Let $\mathbf{H}_{\text{Full}}$ represent the complete CFR measurement with exhaustive RE allocation. Its weighted summation under the Fourier transform basis is:

$$\mathbf{H}_{\text{Full}} = \mathbf{U}\mathbf{Z}\mathbf{V}^{H} = \sum_{m=1}^{M}\sum_{n=1}^{N} \mathbf{u}_m(\mathbf{v}_n)^{H} z_{m,n} = \sum_{m=1}^{M}\sum_{n=1}^{N} \mathbf{\Psi}_{m,n} z_{m,n}, \quad (4)$$

where $\mathbf{u}_m$ and $\mathbf{v}_n$ are the m-th column vector of $\mathbf{U}$ and n-th column vector of $\mathbf{V}$, respectively. $\mathbf{u}_m(\mathbf{v}_n)^{H}$ is the outer product of $\mathbf{u}_m$ and $\mathbf{v}_n$. $\mathbf{\Psi}_{m,n}$ is a unit basis in channel frequency domain, with amplitude 1 on (m, n)-th grid in range-Doppler domain and weighted by path complex gain $z_{m,n}$.

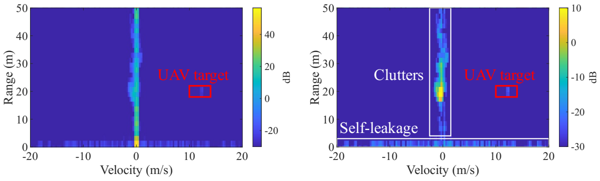

(a) Before. (b) After.

Figure 4: Static background suppression by mean subtraction.

To characterize the occupancy of q REs, we utilize a $\mathbf{W} \in \mathbb{C}^{M \times N}$ as a binary-valued sampling mask with q non-zero entries only at occupied RE positions. Through element-wise multiplication ($\circ$), this mask reserves q measurements from the CFR. A masked CFR measurements $\hat{\mathbf{H}} = \mathbf{W} \circ \mathbf{H}_{\text{Full}}$ can be expressed as:

$$\hat{\mathbf{H}} = \sum_{m=1}^{M}\sum_{n=1}^{N} (\mathbf{W} \circ \mathbf{\Psi}_{m,n})\, z_{m,n} = \sum_{m=1}^{M}\sum_{n=1}^{N} \boldsymbol{\phi}_{m,n} z_{m,n} = \sum_{k=1}^{K} \boldsymbol{\phi}_k z_k, \quad (5)$$

where $\boldsymbol{\phi}_k \in \mathbb{C}^{M \times N}$ denotes the k-th masked atom obtained by re-indexing the double index (m, n) into a single index k. To cast the above model into the compressed sensing form, we vectorize only the q non-zero entries of the masked CFR and each atom as $\hat{\mathbf{h}} \in \mathbb{C}^{q}$ and $\boldsymbol{\phi}_k \in \mathbb{C}^{q}$, which yields $\hat{\mathbf{h}} = \mathbf{\Phi}\mathbf{z}$, where $\mathbf{\Phi} = [\boldsymbol{\phi}_1|\boldsymbol{\phi}_2|\cdots|\boldsymbol{\phi}_K] \in \mathbb{C}^{q \times K}$ is a dictionary formed by vectorized atoms. $\mathbf{z} \in \mathbb{C}^{K}$ is a sparse coefficient vector of z_k.

Accounting for measurement noise in practical scenarios, the reconstruction problem can be formulated as:

$$\hat{\mathbf{z}} = \arg\min_{\mathbf{z}} \|\mathbf{z}\|_0 \quad \text{subject to} \quad \|\hat{\mathbf{h}} - \Phi\mathbf{z}\|_2^2 \leq \varepsilon, \quad (6)$$

where $\|\mathbf{z}\|_0$ is the ℓ_0 pseudo-norm, $\|\cdot\|_2$ denotes the ℓ_2-norm, and ε is a noise tolerance parameter related to the measurement noise level. Our goal is to reconstruct the range-Doppler grid $\mathbf{Z}$ by identifying the complex coefficient vector $\mathbf{z}$ from the noisy observations $\hat{\mathbf{h}}$.

To solve this problem, we employ the 2D-OMP [15], an extension of the standard OMP [48] for 2D sparse signal recovery. The algorithm initializes the residual $\mathbf{R}$ with $\hat{\mathbf{h}}$, and at each iteration k, it selects the atom ϕ_{i_k} that maximizes the correlation with the current residual. The chosen index i_k is appended to the support set $\mathcal{I}_k$. A least-squares update via pseudo-inverse estimates $\hat{\mathbf{z}} = \mathbf{\Phi}_{\mathcal{I}_k}^{\dagger}\hat{\mathbf{h}}$, where $\mathbf{\Phi}_{\mathcal{I}_k}$ is the measurement matrix with only atoms in $\mathcal{I}_k$, and $\mathbf{\Phi}_{\mathcal{I}_k}^{\dagger}$ is the pseudo-inverse of $\mathbf{\Phi}_{\mathcal{I}_k}$. The residual is updated by subtracting $\mathbf{\Phi}_{\mathcal{I}_k}\hat{\mathbf{z}}$ from the observed data. Convergence is declared once the difference between the k-th and $(k-1)$-th residual ratio falls below a threshold or the iteration limit is reached, producing the reconstructed sparse matrix $\hat{\mathbf{Z}}$.

4.2 Dealing with Time-Varying Data Channel

In order to cope with the temporal fluctuations observed in the downlink channel, we first design a quantitative metric *Incoherence-Density Score* to evaluate the channel quality, and then propose *Channel-Adaptive Hierarchical Estimation*, a sensing pipeline that adapts its processing procedure to the instantaneous channel score.

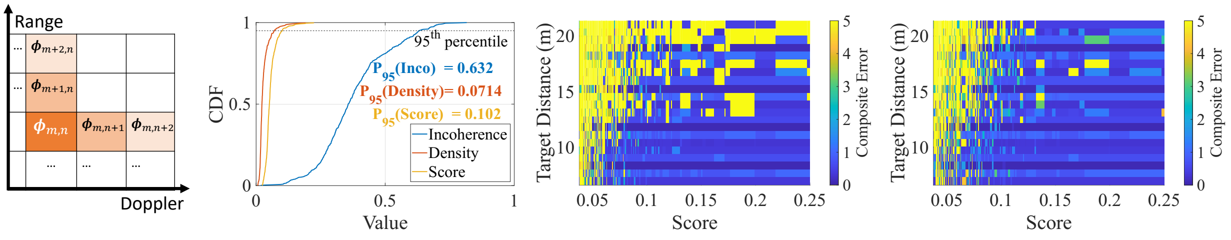

(a) Adjacent atoms. (b) Incoherence-Density distributions. (c) 2D-OMP Composite Error (d) Composite error after suppressing interference.

Figure 5: Score distribution and UAV target sensing performance under different scores.

4.2.1 *Incoherence-Density (ID) Score.* Due to the uncertainty of data transmissions, the sensing capability of 5G signals exhibits temporal variability, demonstrating better performance during periods of dense signal occurrence but compromised accuracy in periods of sparse resource occupancy. To address this dependency, we need to identify intervals conducive to high-quality sensing.

We propose a quantitative metric, named **ID Score**, to evaluate the quality of channel segments. We consider two characteristics that jointly determine the accuracy of range- and velocity-estimation:

(1) Dictionary Incoherence. The way REs are distributed across time–frequency channel resources dictates the achievable range and Doppler resolution. Due to the irregular and non-uniform REs' distribution, the classical Nyquist criterion is no longer valid to indicate how well two targets can be resolved. Instead, we recast the problem as an **incoherence** test on the range-Doppler dictionary: in a compressed-sensing framework, the smaller the mutual coherence among atoms, the more reliably the algorithm separates different scattering paths [24].

Formally, the incoherence $\mu(\Phi)$ is defined as the maximum of all of the distinct pairwise inner products:

$$\mu(\Phi) = \max_{i \neq j} \left| \langle \boldsymbol{\phi}_i, \boldsymbol{\phi}_j \rangle \right|. \tag{7}$$

Although mutual coherence serves as a direct metric, its computational complexity–computing pairwise column correlations–renders it infeasible for real-time applications. To solve this, we propose an efficient approximation method that leverages the regularity of Fourier-based dictionaries:

- *Adjacent atoms' mutual coherence.* Take two adjacent atoms along the range or Doppler axis–for example, the pairs $\langle \boldsymbol{\phi}_{m,n}, \boldsymbol{\phi}_{m+1,n} \rangle$ and $\langle \boldsymbol{\phi}_{m,n}, \boldsymbol{\phi}_{m,n+1} \rangle$ illustrated in Figure 5(a). The step size of the range–Doppler grid defines the finest range and Doppler shift that the system can resolve. The more precisely these atoms can resolve adjacent delays or Doppler shifts, the smaller their mutual coherence (i.e., the magnitude of their inner product) should be.
- *Fourier translation (shift) invariance.* According to the Fourier translation (shift) invariance, any two atoms with the same index difference share the same phase offset, which has the same inner-product magnitude.

Hence, for a given atom $\boldsymbol{\phi}_{m,n}$, we calculate the magnitude of the inner product with its nearest *neighbors* along the delay and Doppler axes. The incoherence is estimated as:

$$\mu(\Phi) = \max\{ |\langle \boldsymbol{\phi}_{m,n}, \boldsymbol{\phi}_{m+1,n} \rangle|, |\langle \boldsymbol{\phi}_{m,n}, \boldsymbol{\phi}_{m,n+1} \rangle| \}, \tag{8}$$

where the larger of these two magnitudes is taken as the incoherence $\mu(\Phi)$ of the current channel snapshot, whereas low values indicate high separability.

(2) Channel-Occupancy Density. A gNB's transmitted power may scale with the number of scheduled resource blocks: with per-RE power being constant, more occupied REs translate into a higher pulse-integrated energy and hence a stronger echo SNR. Therefore, channel-occupancy density ρ is an equally important metric, which is defined as

$$\rho = \frac{q}{M \times N},$$

where q is the number of non-empty REs in the current channel snapshot and $M \times N$ is the total number of REs. ρ is actually proportional to the signal power. High-power intervals are preferred due to their elevated SNR, which enhances target detection robustness by suppressing noise-induced ambiguities in range-Doppler profiles.

To select channel segments that provide both fine delay–Doppler resolution and sufficient energy, the final **ID Score** Ω combines dictionary incoherence $\mu(\Phi)$ and density ρ through a weighted sum:

$$\Omega = (1-\alpha)(1-\mu(\Phi)) + \alpha \cdot \rho. \tag{9}$$

The weighting factor α $(0 \leq \alpha \leq 1)$ is tunable based on operational priorities: higher α emphasizes transmit power or detection range, while lower α prioritizes velocity and range resolution. In *LaSen* setup, we set $\frac{\alpha}{(1-\alpha)}$ according to the ratio between the mean value of measured channel incoherence and density. We analyzed 556 100 ms channel snapshots and computed their density, incoherence, and score. Figure 5(b) shows the distribution of the measured channel occupancy density, incoherence, and score. Only channels with ID scores that exceed a preset threshold (e. g. > 0.1) are identified as a high-score segment.

4.2.2 *Channel-Adaptive Hierarchical Estimation.* To quantify how the channel score affects sensing performance, we evaluated the range and velocity estimation error by applying multiple masks with different scores to the same set of full-band micro-UAV data.

Figure 5(c) illustrates the relationship between the score Ω, UAV target range and composite error[1]. It is shown that sensing with high-score channel segments (score > 0.1) can give accurate distance and velocity estimations. However, according to the score cumulative distributions (shown in Figure 5(b)), the high-score regions constitute merely 5% of the total time duration, while lower-score segments dominate. A sensing strategy that relies only on high-score segments would inevitably suffer from temporal discontinuities. For continuous target sensing under dynamic channel fluctuation, we propose a Channel-Adaptive Hierarchical Global/Local Estimation approach. This algorithm comprises three key components:

1) **Global Estimation** *(Triggered by high-score segments).* As for high-score channel segments, although the reconstruction ability is high, the distant and low-RCS UAV target is weak compared to the strong low-speed clutter and transceiver self-leakage, as shown in Figure 4(b). To avoid the true target being obscured by the residual energy from a strong interferer, instead of reconstructing the range Doppler map from the full dictionary, atoms whose range–Doppler coordinates fall inside the low-speed/short-range region (e.g. $|v| < 1$ m/s, $R < 3$ m) are isolated, as this sector is usually dominated by strong clutter and transceiver self-leakage. The low-speed region can be reconstructed separately if low-speed target detection is needed. Figure 5(d) demonstrates this benefit. Compared with Figure 5(c), we can see that by isolating the low-speed/short-range region from the global estimation, *LaSen* prevents strong interference from masking the weak echoes of distant, small-RCS drones.

2) **Local Estimation** *(Triggered by low-score segments).* As for lower-score channel segments, it can neither provide enough measurement points (due to low density), nor sufficient incoherence among the atoms. This limits the reliability of sensing when using traditional OMP-based approaches. Fortunately, we observe that low-score signal segments do not preclude the feasibility of continuous drone range/velocity estimation: if we limit the search space to a localized vicinity of the target, *the drone's range-Doppler signature becomes statistically distinguishable from ambient interference.* This inspires us to use range/velocity information from previous high-score segments to guide range/velocity estimation in the current frame, thereby improving overall stability. The following are the detailed procedures.

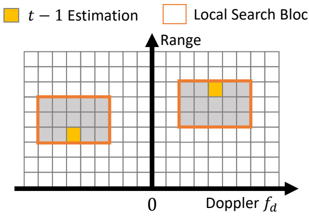

Figure 6: Sketch of block regions in local estimation.

Assume the previous high-score segment yields a dominant component at grid coordinates (m, n) on the range-Doppler map (m for the range, n for Doppler frequency). The kinematic continuity of UAV motion implies a high likelihood of the target persisting within a localized vicinity of (m, n) in the current segment. Thus, we constrain the dictionary's search space to a bounded region $[m \pm \Delta_d, n \pm \Delta_v]$. We can further reduce the search space by considering the target's direction of movement. If the target is moving away from the base station (n is negative), it implies that the distance to the base station is increasing. Thus, the search space is further narrowed to $[m + \Delta_d, n \pm \Delta_v]$; if the target is approaching the base station (n is positive), the space shifts to $[m - \Delta_d, n \pm \Delta_v]$, then the k-th target region B_k in the t-th processing snapshot can be formulated as:

$$\mathcal{B}_k = \left\{(d, v)\ :\ |d - \hat{d}_k| \le \Delta_d,\ |v - \hat{v}_k| \le \Delta_v\right\}, \qquad k = 1, \dots, K_{t-1}, \tag{10}$$

where K_{t-1} represents the total number of target estimates in the last estimation. Figure 6 illustrates this process. In implementation, we choose $\Delta_d = \Delta_v = 2$, which defines a [3.49m, 1.03m/s] bounding box. Each bounded region will independently select the atom with the maximum coefficient. The grid coordinate associated with the largest coefficient magnitude is selected as the estimated target state (range, velocity, and amplitude $(\hat{d}_k, \hat{v}_k, |\hat{z}_k|)$) for the current segment. In subsequent segments, we will start with the new target coordinates as the center and repeat the previous operation. In this way, we can continuously update the target states within low-score segments.

3) **Kalman Filtering.** While constraining the solution space to a localized vicinity of the target enhances robustness of sensing, consecutive estimation errors can induce progressive drift in the solution space, eventually diverging from the true target state. To mitigate this error propagation, *LaSen* employs Kalman filtering with a dynamic measurement noise matrix $\mathbf{R}$. Its core idea is to dynamically balance the weighting between predictions and estimations under a fluctuating channel: assigning greater weight to the estimation when the ID score is high, otherwise relying more on the prediction.

The Kalman filter predicts a state $d'_{t|t-1}$, $v'_{t|t-1}$ from the model and then corrects it with the new estimation $\hat{d}_t$, $\hat{v}_t$. The weight of that correction is the *Kalman gain* [19]:

$$K_t = P_{t|t-1} A^{\mathsf{T}} \left(A\, P_{t|t-1} A^{\mathsf{T}} + R\right)^{-1}, \tag{11}$$

where $P_{t|t-1}$ is the predicted covariance, A is the measurement matrix and R is the measurement-noise covariance. When R is small, representing a reliable current estimation, K_t will grow, and thus the filter trusts the estimation; when R is large, representing a noisy current estimation, K_t will shrink, and correspondingly, the filter relies mainly on the model prediction. R governs the filter's ability to balance the influence of new estimates against prediction, ensuring the final state is the best compromise between prediction and noisy data.

In *LaSen*, the t-th measurement-noise covariance used by the Kalman filter is adaptively interpolated between two limits,

$$\mathbf{R}_t(\Omega_t^*) \;=\; (1 - \Omega_t^*)\,\mathbf{R}_{\max} \;+\; \Omega_t^*\,\mathbf{R}_{\min}, \tag{12}$$

where the normalized channel score $\Omega_t^* \in [0, 1]$ gauges the instantaneous sensing quality. Ω_t^* is defined as $\Omega_t^* = \min(\dfrac{\Omega_t}{\Omega_{\text{thr}}}, 1)$,

---

[1] Here, the composite error is defined as $\sqrt{\Delta d^2 + \Delta v^2}$ (in Section 6), aiming to show the range and velocity deviation simultaneously.

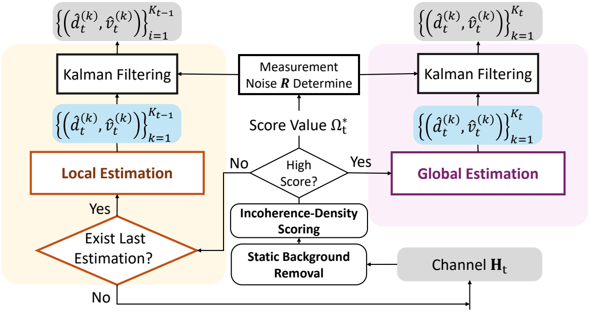

Figure 7: Channel-adaptive hierarchical estimation design flow.

where Ω_t is the raw score of the t-th snapshot, Ω_{thr} is the preset "high-quality" threshold. The two bounding matrices are

$$\mathbf{R}_{min} = \begin{bmatrix} \delta_d^2 & 0 \\ 0 & \delta_v^2 \end{bmatrix}, \quad \mathbf{R}_{max} = \begin{bmatrix} \Delta_d^2 & 0 \\ 0 & (2\Delta_v)^2 \end{bmatrix}, \tag{13}$$

where δ_d, δ_v are the range- and Doppler-grid spacings and Δ_d, Δ_v the half-widths of the local search region. In *LaSen*, during the high-score interval, the global estimation is considered reliable, and thus the estimation noise is approximated as the square of range and Doppler resolution; while during the low-score interval, the largest estimation noise is approximated as the square of the maximum bounding range.

Consequently, when the channel is poor for sensing ($\Omega_t^* \approx 0$), Eq. (12) assigns the larger covariance $\mathbf{R}_{\text{max}}$, forcing the filter to rely more on the prediction; when the channel is suitable for sensing ($\Omega_t^* \approx 1$), the filter trusts the observation and uses $\mathbf{R}_{\text{min}}$. Thus, *LaSen* yields a smooth interpolation between the extremes. Figure 7 gives the design flow of the channel-adaptive hierarchical estimation scheme.

5 Implementation

We implement *LaSen* on an NI USRP-2954R software-defined radio [38], which combines two daughterboard slots and supports duplex transmitting and receiving. To maximize RF isolation between the single-TX and single-RX chains, we utilize separate daughterboard slots for transmission and reception. The transmitter is attached with a power amplifier and a 12 dBi panel antenna. The SDR platform conducts transmission/reception tests at 5.8 GHz unlicensed band, with transmission power within 24.9 dBm. A 10 dBi Yagi antenna is used to enhance the receiver directional gain, and a shielding plate at the receiver antenna is used to reduce direct leakages between the antennas. A GPS-disciplined Network Time Protocol server is used to synchronize the host and the drone's Real-Time Kinematic (RTK) positioning results.

Waveform generation and configuration. We generate the 5G NR waveform using the MATLAB 5G toolbox [35]. To simulate the operational configurations of practical base stations, we analyzed the System Information Block 1 (SIB1) transmitted by an N41 band base station using Wireshark. Based on the base station's configurations of subcarrier spacing, Physical Downlink Shared Channel (PDSCH), and Demodulation Reference Signals (DM-RS), we generated similar waveforms in MATLAB to ensure the resource allocation pattern is compliant with real-world 5G NR configurations. The PDSCH payload is filled with pseudo-random bit sequences, and the modulation type of the data symbol is QPSK. We generate the waveform under the 92.16 MHz sampling rate with 3072 FFT points and 30 kHz SCS[2]. The carrier bandwidth is 78.12 MHz, where each symbol contains 2604 non-empty subcarriers and 468 guard-band subcarriers.

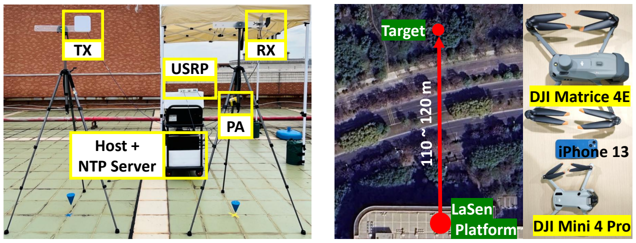

(a) Experiment setup. (b) Rooftop scenario and targets.

Figure 8: Hardware setup and experiment scenario.

Backend processing. We employ MATLAB 2024b for implementing *LaSen*. The captured signal is stored in the USRP's onboard 1 GB DDR3 memory and then transferred to a host via a 10 GbE Network Adapter for offline processing. The captured waveforms are correlated with the transmitted waveform to enable synchronization, and then demodulated into a resource grid structure. The resource grid undergoes the element division operation in Equation (1) to derive the channel frequency response. The signal processing window is 100 ms, and the range-velocity estimation interval is 50 ms. The entire signal processing chain is executed on a host equipped with an Intel Core i7-13700K processor and 64 GB RAM.

6 Evaluation

In this section, we evaluate the proposed *LaSen* performance under different settings to show the feasibility of UAV target sensing under the practical NR downlink resource allocation.

6.1 Experiment Design

6.1.1 Data Collection. We conduct experiments under two different outdoor scenarios. The first one is on the rooftop of a building (Figure 8(b)), emulating the real-world base station deployment, and the other one is on a lawn (Figure 17(a)), evaluating the impact of multiple background targets. We evaluate *LaSen* using two drones: DJI Matrice 4E [12] with a size of 307 mm × 388 mm × 150 mm and a maximum speed of 21 m/s and DJI Mini 4 Pro [13] with a size of 298 mm × 373 mm × 101 mm and a maximum speed of 14 m/s.

During flying, *LaSen* continually transmits NR signals with full resource allocation while simultaneously activating the receiver for capturing. For simplicity, hereafter we refer to this configuration as

---

[2] We note SCS of 30 kHz is typically used in NR FR1 band. Although changing the SCS alters the maximum unambiguous range and velocity, the performance of target sensing depends more on the occupied resource pattern than on the SCS itself, as shown in Section 6.3.

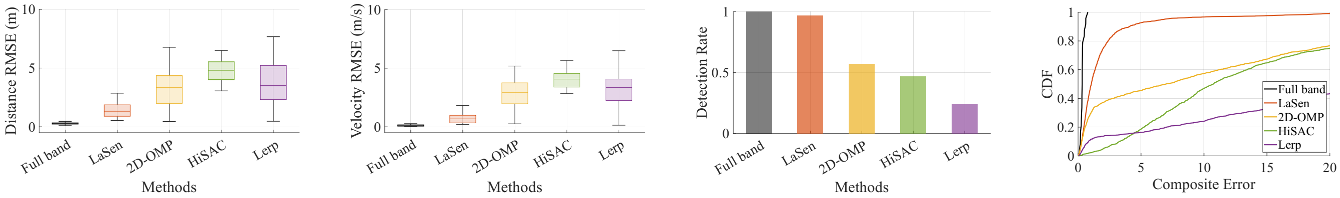

(a) Distance Error.

(b) Velocity Error.

(c) Detection Rate.

(d) Composite Error.

Figure 9: Overall Performance.

the "full-band" mode. We collect over 1335 range-velocity estimates across 35 separate trajectories.

We capture and demodulate 2200 data frames from two China Mobile N41 band gNBs in our campus, which contain the 100 MHz allocated bandwidth. We reserve the resource grid with a subcarrier range from RE 0 to RE 2603. The measurement environment includes locations with different traffic volumes. We use the maximum power within an SSB group as a threshold T_{ssb}. Resource grids with energy ±10 dB of T_{ssb} were identified as occupied resources in the measurement direction, resulting in a binary mask indicating the RE occupation pattern. The final channel frequency response was obtained by performing element-wise multiplication between the full-band drone measurements and the derived occupancy masks, generating 12079 channel samples for further analysis.

6.1.2 Baseline Methods. To comprehensively evaluate the *LaSen* performance, we adopt the following baseline methods for comparison:

2D-OMP [15]. The default 2D-OMP method reconstructs the range-Doppler profile by greedily searching for the strongest atom until the k-th and $(k-1)$-th residual ratio falls below a threshold (i.e., 10^{-5}), or reaches the maximum iteration limit (i.e., 50).

HiSAC [39]. For comparison with frequency-domain sparse recovery methods, we reproduce the HiSAC approach in a single-system scenario. Temporal coherent aggregation is applied over 7-symbol intervals (0.25 ms) to maintain phase coherence and improve ranging accuracy. Then the CIR is reconstructed on each aggregated OFDM symbol using OMP. To accommodate high noise levels in the measurements, the reconstruction error threshold is set to 0.85. We have made the following adjustments based on the HiSAC to handle resource fluctuations and ensure numerical stability: if an insufficient number of measurements causes the invertibility of $(\mathbf{\Phi}_{\mathcal{I}_k}^H \mathbf{\Phi}_{\mathcal{I}_k})$ to become numerically unstable (reciprocal condition number < 0.01), OMP terminates early. The time domain linear interpolation is applied to the per-frame CIR estimates to mitigate velocity-domain spectral leakage caused by non-uniform time resource allocation.

Lerp [8]. The linear interpolation approach enables continuous estimation by leveraging neighboring active OFDM symbols. Then the range–Doppler profile is calculated by 2D-FFT using the interpolated grids.

To ensure fair comparison, we use the same Constant False Alarm Rate (CFAR) detector and Kalman filter for baselines. 2D-OMP doesn't need to use a CFAR detector due to its reconstruction characteristics. All methods are initialized using the same high-score occupancy mask, with initialization results excluded from the error analysis.

6.1.3 Evaluation Metrics. To ensure a fair and comprehensive evaluation, we adopt three primary metrics: Root Mean Squared Error (RMSE), Composite Error (CE), and Detection Rate (DR). RMSE quantifies the estimation accuracy of a drone's distance and velocity. We use centimeter-level RTK positioning as the ground truth for single-target scenarios. For multi-target evaluations where RTK is partially unavailable, we adopt high-fidelity full-band measurements (with a distance/velocity RMSE of 0.3 m and 0.1 m/s) as the benchmark. CE is introduced as an empirical metric to characterize the joint estimation error in both range and velocity domains, defined as $CE = \sqrt{\Delta d^2 + \Delta v^2}$, where Δd and Δv denote the respective estimation residuals. DR measures detection robustness, defined as the ratio of correctly detected targets to the total number of targets identified by the full-band benchmark. A target is considered correctly detected if its CE is below a threshold of 10. In our analysis, DR and RMSE are considered jointly to provide a holistic view.

6.2 Overall Performance

We compare the performance of *LaSen* with the full-band and other baseline methods under varying downlink channel occupancy conditions. As shown in Figure 9, *LaSen* performs the closest to the full-band method among all approaches. The median RMSE for distance and velocity estimation are 1.06 m and 0.34 m/s, respectively. Compared to the full-band results, whose median RMSE of distance is 0.30 m and velocity is 0.10 m/s, *LaSen* only increases approximately twice the full-band error under an average channel occupancy of just 3%. Additionally, *LaSen* reduces distance errors by 51.84% and velocity errors by 82.84% compared to 2D-OMP, demonstrating its robustness against fluctuating channel conditions.

HiSAC achieves a higher detection rate than Lerp, indicating its better utilization of limited bandwidth in sparse resource scenarios. However, the composite-error CDF in Figure 9(d) shows that for the majority of scenarios, HiSAC returns higher errors than others. This indicates that the one-dimensional sparse model in HiSAC struggles to adapt to resource dynamics. For *LaSen*, 80% of composite errors are confined within 2.38, outperforming all other methods. These results collectively indicate the system's capability to approach full-band estimation accuracy while adapting to target kinematics and channel variability.

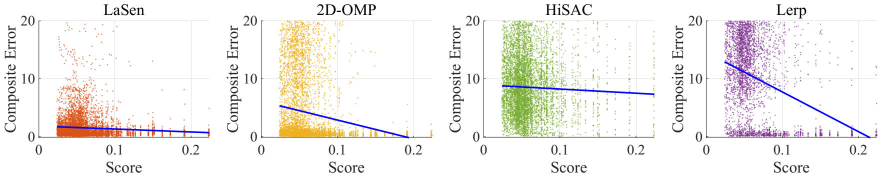

Figure 10: Performance comparison under different scores.

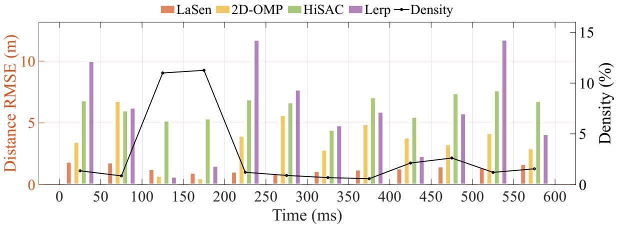

Figure 11: Performance comparison of different data traffic.

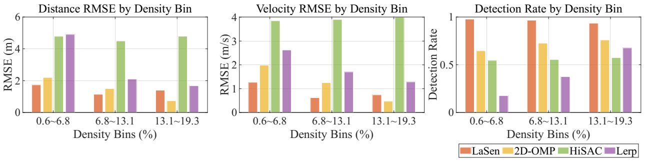

Figure 12: Results under different occupancy density.

6.3 Evaluation on Time-varying Channels

We investigate how the time-varying channel influences range and velocity estimation.

Score. We calculate the score of consecutive channel segments and the corresponding target range/velocity estimation errors under those channels. We use composite error to simultaneously capture the range and velocity deviation, as shown in Figure 10. We superimpose a blue line onto the fitted data to emphasize overall trends. The results are clear-cut: *LaSen* outperforms every baseline in both the high-score region (score > 0.1) and the low-score region (score < 0.1). In particular, when the score is below 0.1, the error spread of *LaSen* is markedly smaller than that of the other three methods. Among the baselines, 2D-OMP has more points concentrated in the low composite error region, showing less sensitivity to score variations than HiSAC and the Lerp, confirming the advantage of 2D compressed-sensing under non-uniform channel sampling. Building on this, *LaSen* further reduces the low-score error by local searches around detected targets.

It can be seen that in some cases with a high score (score > 0.1), there also appear some relatively high error estimations. This is due to the weak reflections from a faraway target. In this case, the impact of channel fluctuation is no longer significant. Therefore, for targets whose distances are within the detection range, *LaSen* can effectively mitigate the influence of low-score channels on estimation accuracy while suppressing distortions induced by channel fluctuations.

Data Traffic. To analyze the impact of the data traffic pattern, we evaluate the *LaSen* performance under varying traffic loads. Figure 11 shows the distance RMSE over a 600ms gNB recording in Figure 3(b). The signal-processing window is 100ms, and the range–velocity estimation interval is 50ms. The bar plots show per-interval distance RMSE for *LaSen* and baselines, while the black curve represents the resource-occupancy density in each interval. It can be found that intervals with low occupancy density tend to induce larger RMSEs for all methods. This is most pronounced when the occupied subcarriers are sparse and concentrated in narrow frequency portions, which degrade range-domain reconstruction and reduce the effective SNR available for sensing. Among baselines, *LaSen* degrades far more gracefully: its RMSE remains low across most intervals and exhibits substantially smaller variance than competing methods, indicating greater robustness to variations in data traffic patterns.

Occupancy Density. We analyze the impact of NR channel occupancy density on UAV sensing performance across three density bins: sparse (0.6%–6.8%), moderate (6.8%–13.1%), and dense (13.1%–19.3%). As shown in Figure 12, *LaSen* maintains consistently low distance and velocity RMSE across all density conditions, demonstrating its robustness to resource sparsity. In contrast, baseline methods exhibit higher errors under sparse resource conditions. Specifically, HiSAC incurs the largest velocity RMSE and shows limited performance scaling with increasing resource density, indicating that one-dimensional sparse recovery is fundamentally limited under time-frequency non-uniform resource allocation.

6.4 Evaluation on Target Issues

Distance. We investigate how the target-to-transceiver distance affects sensing accuracy and detection probability. Figure 13 summarizes the results in three distance bins. Within the 6-74 m, *LaSen* achieves a relatively lower RMSE in both range and velocity, clearly outperforming baselines. The distance estimation error of *LaSen* increases with target range. For distant UAVs, since the average of occupied signals accounts for only 3% of the full band, the gap to an ideal full-band configuration becomes wider as the reflection signal energy decreases with range. As for the detection rate, *LaSen* retains the highest detection probability across the whole distance range. This is because if the Kalman filter could converge, *LaSen* can maintain a correct local estimation region by prediction even when new observations are sporadic. However, the absence of reliable updates gradually enlarges its estimation error, which explains the increase of distance and velocity RMSE at 74-108 m.

Velocity. We next examine how the absolute target speed influences sensing accuracy and detection probability. Figure 14 groups

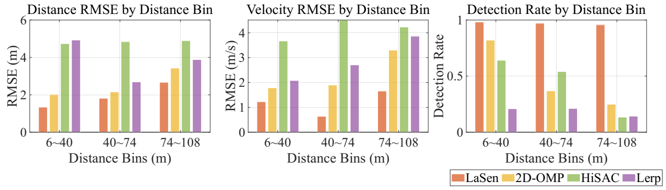

Figure 13: Results under different UAV Target Distance.

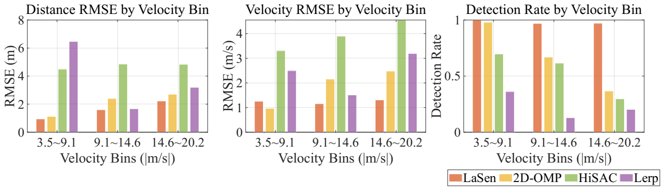

Figure 14: Results under different UAV Target Velocity.

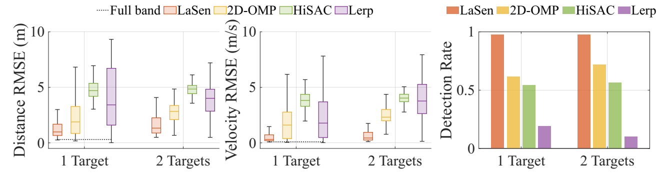

Figure 15: Comparison of different numbers of targets.

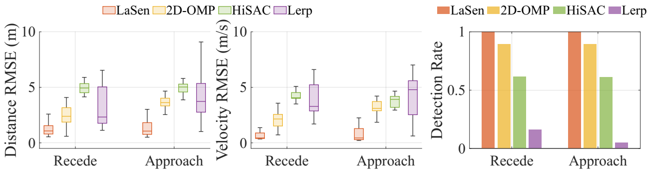

Figure 16: Comparison of different directions.

the results into three velocity bins. As target speed increases, the estimation errors of *LaSen* for both distance and velocity rise. This is because, in the experiments with high-speed UAVs, the targets were accelerated from nearby starting positions. Compared to other methods, *LaSen* demonstrates the most stable estimation and detection performance across different velocity bins, with particularly minimal variation in velocity estimation errors. Within the 14.6–20.2 m/s speed interval, the distance and velocity RMSE for *LaSen* is 2.2 m and 1.3 m/s.

We note there are two groups of CSI-RS resource set in the measured N41 gNB channel, with a period of 10 ms and an offset of 5 ms, achieving a maximum sampling rate of 200 Hz. At the same 5.8 GHz frequency setting, the method based on CSI-RS estimation has an unambiguous velocity range of up to 2.6 m/s, while *LaSen* extends this range to 20.2 m/s. We did not measure the maximum speed sensing range of *LaSen*, since the upper speed limit of the drone is 21 m/s.

Target Number. We evaluate *LaSen* using two drones of different sizes in a multi-drone scenario. The horizontal distance between the two drones during hovering was approximately 5 m, after which they simultaneously accelerated away from or towards the antenna. Figure 15 presents the performance comparison. The estimation errors of baseline methods consistently increase in distance and velocity in the two-target scenario compared to the single-target scenario. This observation reflects that accurately detecting multiple targets is challenging due to variations in relative distances and velocities between targets. In contrast, *LaSen* demonstrated minor performance degradation between single and dual-drone setups, outperforming all baseline methods in both cases. Specifically, the median distance and velocity estimation errors for *LaSen* with two drones were 1.33 m and 0.44 m/s. Comparing *LaSen* with 2D-OMP method, *LaSen* boosts the detection rate by 26% and decreases the range- and velocity-estimation errors by 53% and 81%, respectively. It demonstrates that *LaSen* can effectively mitigate the effects of channel fluctuations.

Direction of multiple targets. We evaluate how the UAV direction will impact the sensing performance. Two drones perform flight operations in opposite directions. The receding trajectory is starting from 24 m to 52 m, while the approaching trajectory is starting from 40 m to 20 m. Figure 16 illustrates the performance comparison of targets' receding and approaching. Compared with other methods, *LaSen* has a similar sensing performance under different target moving directions. For target receding, the distance and velocity RMSE are 1.08 m and 0.44 m/s, while for target approaching, the distance and velocity RMSE are 1.06 m and 0.44 m/s. When the UAV flies away, if it is first detected at a close range with a high-score frame, this accurate estimation allows *LaSen* to keep its local-search window closely following the target until the target moves beyond the detection range, yielding robustness to channel fluctuations. Similarly, if the UAV approaches from afar, as long as the target reflection power is above the detection threshold, *LaSen* can obtain an accurate range/velocity estimation when at least one high-score snapshot occurs.

Multiple Moving Target Interference. To analyze the impact of multiple moving targets in a realistic environment, we conduct experiments in an outdoor location featuring nearby streets, as illustrated in Figure 17(a). Figure 17(b) and Figure 17(c) show the range and velocity trajectories of the drone and non-cooperative vehicles captured during the acquisition period under the full-band configuration and *LaSen*, respectively. Targets detected around the zero-frequency region might include pedestrians or trees. In contrast, *LaSen* mitigates the interference of those nearly stationary targets by employing dictionary partitioning in its global estimation step (Section 4.2.2). Comparing the results of *LaSen* with the full-band approach, it demonstrates that the presence of multiple moving targets in practical scenarios does not significantly affect the *LaSen*'s accuracy, showing the robustness of *LaSen* under multiple different kinds of moving targets.

7 Related Work

UAV Detection and Tracking. Robust and efficient sensing of UAVs is critical for low-altitude security. Vision-based methods employ optical or thermal cameras to identify drones [14, 36], offering cost-effective, high-resolution imaging at close range but suffering from environmental sensitivity. Acoustic techniques analyze distinctive spectral features from rotor sounds [20, 21, 44],

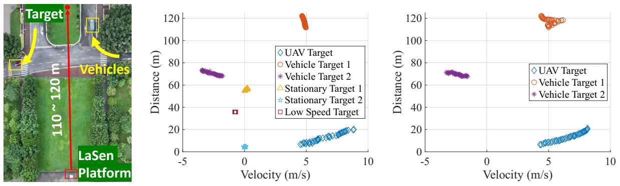

(a) Scenario. (b) Full band. (c) LaSen.

Figure 17: Multiple moving targets range-velocity estimation.

enabling all-weather operation but remaining constrained by ambient noise and limited detection range. Multi-modal systems that combine vision and acoustic sensors can enhance detection accuracy and reliability through data fusion [7, 47]. However, such integrated systems may collect extensive information and raise privacy concerns. RF-based identification focuses on identifying the communication signals emitted by UAVs and their controllers from ambient interference and noise [6, 9, 51]. However, this approach fails when no communication is present between the UAV and its controllers [43]. Radar [23, 27, 42, 52] and LiDAR [4] systems can locate drones by transmitting radio waves and examining the reflected signals to determine their position, speed, and altitude. However, wide-area deployment is expensive for radar. The low-cost LoRa signals can also be employed for long-range UAV detection via pulse concentration[50], but its limited bandwidth and a low pulse repetition frequency prevent accurate drone localization and velocity estimation. Compared to these methods, gNBs are widely deployed with high transmission power and sufficient bandwidth (up to 100 MHz), demonstrating considerable potential for UAVs detection and tracking.

Base Station based Wireless Sensing. The emergence of ISAC has driven significant research efforts in wireless sensing using 5G NR or LTE frameworks. Existing approaches mainly fall into three categories: custom waveform designs [22, 31], reference signal utilization [5, 10, 11, 17, 18, 25, 28, 37, 40, 41, 49], and downlink data signal utilization [34, 45]. LTE-based solutions typically derive Doppler information from the 1 kHz CRS [11, 17, 46], whereas 5G NR adopts CSI-RS for enhanced spectral efficiency. Leveraging commodity gNB CSI-RS, Chen et al. [10] demonstrate rotational motion detection using commercial gNB CSI-RS. It also reveals that the unambiguous velocity is bounded by the CSI-RS repetition period. Recent studies try to extend this bound by fusing multiple reference signals (CSI-RS/DM-RS/PRS) [25, 37, 49], yet facing implementation challenges: DM-RS exhibits temporal unpredictability due to burst data traffic coexistence, while PRS availability depends on UE positioning requests. Those traffic uncertainties are seldom addressed in prior work [25, 37, 45, 49]. Emerging research identifies that live-traffic variability can degrade sensing performance [34]: to mitigate this, the drone detection process is executed when the resource grid is nearly fully occupied. In contrast, our measurements reveal that, for a given gNB, less than 5% of total time duration exhibits a resource-utilization density above 7.1% (Figure 5(b)). Restricting sensing to these rare high-occupancy intervals may impose frequent and prolonged sensing outages. To our knowledge, *LaSen* presents the first practical NR downlink resource-aware compressive sensing framework that achieves continuous target tracking with volatile signal patterns.

Sparse Recovery in Wireless Sensing. The limited bandwidth of communication systems typically constrains sensing resolution. To overcome this limitation, a number of studies have focused on expanding the sensing bandwidth by aggregating discrete channel responses [29, 30, 39]. HiSAC [39] is a multiband ISAC system that aggregates communication traffic across multiple bands to boost the sensing resolution. It addresses the non-contiguity and high sparsity of communication subbands, as well as their incoherent phase offsets. In [29], Li *et al.* proposed UWB-Fi, which randomly hops through available Wi-Fi channels and leverages discrete and irregular channel sampling to expand WiFi bandwidth and can achieve fine-granularity sensing. Similarly, in [30], the authors propose CCS-Fi, a compressive channel sampling framework for Wi-Fi sensing. Different from existing works, *LaSen* mainly tackles the volatile signal patterns in 5G NR.

8 Discussion

In this section, we discuss some practical issues during the implementation of *LaSen*.

Target Angle Estimation. *LaSen*'s current implementation focuses on resolving the range-Doppler profile of UAVs, as our SDR prototype (NI USRP X310) has only two receiving channels, limiting angular resolution for angle-of-arrival (AoA) estimation. Commercial 5G-NR gNBs typically deploy large antenna arrays (e.g., 4 × 4, 8 × 8), enabling high-resolution AoA estimation. With such deployments, *LaSen*'s sensing framework can seamlessly integrate with existing MUSIC/ESPRIT-based AoA estimation to provide full 3D localization (range, velocity, and azimuth/elevation).

Extreme Scenarios with No High-Quality Segments. In extreme cases where all channel segments exhibit ultra-low utilization, the system risks performance degradation due to no reliable initialization: the newly appearing targets may be missed, and errors could accumulate. To address this, the gNB can dynamically insert sensing-dedicated reference signals (e.g., PRS) into idle resource blocks, enhancing the measurement matrix without affecting user traffic and thereby ensuring robust initialization and maintaining full compliance with 5G-NR standards.

Effects of Multipath and Target Discrimination. Strong static multipaths from ground and buildings can mask small-RCS targets through shadowing effects. Beyond the static background removal technique introduced in Section 4.1.1, an auxiliary receiver equipped with multiple antennas can adopt beamforming strategies to suppress interference from non-target directions. As the number of UAVs increases or dynamic clutter such as birds is introduced, the system can coordinate with neighboring ISAC stations to perform joint data fusion, thereby mitigating mutual interference among targets while enhancing spatial discrimination capability. Furthermore, dynamic clutter can lead to false alarms and increase unnecessary local estimation overhead. One potential solution is to reduce the window length and step size to extract micro-Doppler signatures in the target's range profile. The signature produced by UAV rotor blades could effectively distinguish drones from other non-cooperative targets [26].

Inter-Cell and Intra-Cell Interference. Inter-cell interference primarily arises from neighboring cells transmitting on overlapping time-frequency resources, which can raise the noise floor or create spurious peaks in received signals. To mitigate these effects, receiver-side null-steering beamforming can place spatial nulls in the direction of dominant interference [33], effectively rejecting strong inter-cell signals. In mono-static sensing architectures, the intra-cell interference happens when transmitter leakage into the receiver chain, which can saturate front-end components and degrade UAV detection performance. In the current implementation of *LaSen*, we employ a straightforward but effective passive isolation strategy. This involves two key measures: a conductive shielding plate between the transmitter and receiver antennas to mitigate near-field coupling, and a static background removal algorithm to suppress residual self-interference. While this approach suffices for proof-of-concept validation under controlled conditions, practical deployments would benefit from advanced active cancellation techniques, such as analog or digital domain interference subtraction [8], which can achieve >50 dB suppression in full-duplex OFDM systems.

9 Conclusion

In this paper, we present *LaSen*, an integrated sensing and communication scheme for tracking low-altitude UAVs using 5G NR signals. *LaSen* jointly leverages periodic reference signals and stochastic downlink data transmissions for sensing. It formulates the tracking of UAVs as a sparse recovery problem, where target range and Doppler are directly reconstructed from non-uniform, sub-Nyquist samples. A channel-adaptive hierarchical framework is designed to address the challenges arising from volatile 5G signal patterns, significantly enhancing sensing reliability and continuity under time-varying channels. We believe that *LaSen* demonstrates the feasibility of sensing high-mobility targets within next-generation dual-function 5G/6G infrastructures.

Acknowledgments

This work was supported in part by the Guangdong S&T Programme under Grant 2024B0101020004; in part by the National Natural Science Foundation of China under Grant 62472452, T2495254; in part by Guangdong Basic and Applied Basic Research Foundation (No. 2025A1515010262, 2023B1515120058); in part by RGC under AoE/E-601/22-R; in part by SUSTech Fang Keng Faculty Award; in part by the Center for Computing Science and Engineering at Southern University of Science and Technology. Q. Huang and J. Zhang are the corresponding authors.

References

[1] 2025. Global Drone Market Report 2025-2030.

[2] 3GPP. 2020. NR; Physical channels and modulation (Release 16). https://www.3gpp.org/ftp/Specs/archive/38_series/38.211/ V16.2.0 (2020-07).

[3] 3rd Generation Partnership Project. 2025. *Radio Resource Control (RRC) protocol specification.* Technical Specification Group Radio Access Network TS 38.331. 3GPP. https://portal.3gpp.org/desktopmodules/Specifications/SpecificationDetails.aspx?specificationId=3197 Release 19.

[4] Tasnim Azad Abir, Vu Le, Endrowednes Kuantama, Pranjol Sen Gupta, Austin Copley, Judith Dawes, Mohammad Islam, Richard Han, and Phuc Nguyen. 2025. Detection and Tracking of Drone Swarms using LiDAR. In *Proceedings of the 23rd Annual International Conference on Mobile Systems, Applications and Services.* 500–514.

[5] Karol Abratkiewicz, Adam Księżyk, Marek Płotka, Piotr Samczyński, Jacek Wszołek, and Tomasz Piotr Zieliński. 2023. SSB-based signal processing for passive radar using a 5G network. *IEEE Journal of Selected Topics in Applied Earth Observations and Remote Sensing* 16 (2023), 3469–3484.

[6] Mohammad F Al-Sa'd, Abdulla Al-Ali, Amr Mohamed, Tamer Khattab, and Aiman Erbad. 2019. RF-based drone detection and identification using deep learning approaches: An initiative towards a large open source drone database. *Future Generation Computer Systems* 100 (2019), 86–97.

[7] Ildi Alla, Hervé B Olou, Valeria Loscri, and Marco Levorato. 2024. From sound to sight: Audio-visual fusion and deep learning for drone detection. In *Proceedings of the 17th acm conference on security and privacy in wireless and mobile networks.* 123–133.

[8] Carlos Baquero Barneto, Taneli Riihonen, Matias Turunen, Lauri Anttila, Marko Fleischer, Kari Stadius, Jussi Ryynänen, and Mikko Valkama. 2019. Full-duplex OFDM radar with LTE and 5G NR waveforms: Challenges, solutions, and measurements. *IEEE Transactions on Microwave Theory and Techniques* 67, 10 (2019), 4042–4054.

[9] Sanjoy Basak, Sreeraj Rajendran, Sofie Pollin, and Bart Scheers. 2021. Combined RF-based drone detection and classification. *IEEE Transactions on Cognitive Communications and Networking* 8, 1 (2021), 111–120.

[10] Penghui Chen, Liuyang Tian, Yujing Bai, and Jun Wang. 2024. Rotating Target Detection Using Commercial 5G Signal. *Applied Sciences* 14, 10 (2024), 4282.

[11] Weiyan Chen, Kai Niu, Deng Zhao, Rong Zheng, Dan Wu, Wei Wang, Leye Wang, and Daqing Zhang. 2020. Robust dynamic hand gesture interaction using LTE terminals. In *2020 19th ACM/IEEE International Conference on Information Processing in Sensor Networks (IPSN).* IEEE, 109–120.

[12] DJI. 2025. *DJI Matrice 4 Series.* https://enterprise.dji.com/cn/matrice-4-series/specs Official technical specifications for DJI Matrice 4 drone.

[13] DJI. 2025. *DJI Mini 4 Pro.* https://www.dji.com/cn/mini-4-pro/specs Official technical specifications for DJI Mini 4 Pro drone.

[14] Yifei Dong, Fengyi Wu, Sanjian Zhang, Guangyu Chen, Yuzhi Hu, Masumi Yano, Jingdong Sun, Siyu Huang, Feng Liu, Qi Dai, et al. 2025. Securing the Skies: A Comprehensive Survey on Anti-UAV Methods, Benchmarking, and Future Directions. In *Proceedings of the Computer Vision and Pattern Recognition Conference.* 6659–6673.

[15] Yong Fang, JiaJi Wu, and BorMin Huang. 2012. 2D sparse signal recovery via 2D orthogonal matching pursuit. *Science China Information Sciences* 55 (2012), 889–897.

[16] Federal Aviation Administration. 2020. *Small Unmanned Aircraft Systems (UAS) Regulations (Part 107).* https://www.faa.gov/newsroom/small-unmanned-aircraft-systems-uas-regulations-part-107

[17] Yuda Feng, Yaxiong Xie, Deepak Ganesan, and Jie Xiong. 2021. LTE-based pervasive sensing across indoor and outdoor. In *Proceedings of the 19th ACM Conference on Embedded Networked Sensor Systems.* 138–151.

[18] Yuda Feng, Yaxiong Xie, Deepak Ganesan, and Jie Xiong. 2022. Lte-based low-cost and low-power soil moisture sensing. In *Proceedings of the 20th ACM Conference on Embedded Networked Sensor Systems.* 421–434.

[19] Mohinder S Grewal and Angus P Andrews. 2014. *Kalman filtering: Theory and Practice with MATLAB.* John Wiley & Sons.

[20] Junfeng Guo, Ishtiaq Ahmad, and KyungHi Chang. 2020. Classification, positioning, and tracking of drones by HMM using acoustic circular microphone array beamforming. *EURASIP Journal on Wireless Communications and Networking* 2020, 1 (2020), 9.

[21] Yuan He, Weiguo Wang, Luca Mottola, Shuai Li, Yimiao Sun, Jinming Li, Hua Jing, Ting Wang, and Yulei Wang. 2023. Acoustic localization system for precise drone landing. *IEEE Transactions on Mobile Computing* 23, 5 (2023), 4126–4144.

[22] Yinghui He, Guanding Yu, Zhenzhou Tang, Jianfeng Wang, and Haiyan Luo. 2024. A Dual-Functional Sensing-Communication Waveform Design Based on OFDM. *IEEE Transactions on Wireless Communications* 23, 11 (2024), 16962–16975. doi:10.1109/TWC.2024.3448456

[23] Yuan He, Jia Zhang, Rui Xi, Xin Na, Yimiao Sun, and Beibei Li. 2024. Detection and identification of non-cooperative uav using a cots mmwave radar. *ACM Transactions on Sensor Networks* 20, 2 (2024), 1–22.

[24] Matthew A Herman and Thomas Strohmer. 2009. High-resolution radar via compressed sensing. *IEEE transactions on signal processing* 57, 6 (2009), 2275–2284.

[25] Keivan Khosroshahi, Philippe Sehier, and Sami Mekki. 2024. Leveraging PRS and PDSCH for integrated sensing and communication systems. In *GLOBECOM 2024-2024 IEEE Global Communications Conference.* IEEE, 4702–4707.

[26] Harish C Kumawat, Piotr Samczyński, et al. 2022. Spectrum localization and hough transform-based β tuning for LSS targets' accurate micro-Doppler imaging system. *IEEE Transactions on Instrumentation and Measurement* 71 (2022), 1–11.

[27] Maisy Lam, Laura Dodds, Aline Eid, Jimmy Hester, and Fadel Adib. 2025. 6D Self-Localization of Drones Using a Single Millimeter-Wave Backscatter Anchor. In *IEEE INFOCOM 2025-IEEE Conference on Computer Communications.* IEEE, 1–10.

[28] Hang Li, Yang Xiang, Qinghua Guo, Lizhe Liu, Xiaojing Huang, Zhiqun Cheng, and Yashan Pang. 2025. An Efficient Direct Downlink Sensing Method Using 5G

NR SSB Signals in Perceptive Mobile Networks. *IEEE Internet of Things Journal* (2025).

[29] Xin Li, Hongbo Wang, Zhe Chen, Zhiping Jiang, and Jun Luo. 2024. Uwb-fi: Pushing wi-fi towards ultra-wideband for fine-granularity sensing. In *Proceedings of the 22nd Annual International Conference on Mobile Systems, Applications and Services*. 42–55.

[30] Xin Li, Hongbo Wang, Jingzhi Hu, Zhe Chen, Zhiping Jiang, and Jun Luo. 2025. CCS-Fi: Widening Wi-Fi Sensing Bandwidth via Compressive Channel Sampling. In *Proceedings of IEEE International Conference on Computer Communications*.

[31] Fan Liu, Ya-Feng Liu, Yuanhao Cui, Christos Masouros, Jie Xu, Tony Xiao Han, Stefano Buzzi, Yonina C Eldar, and Shi Jin. 2025. Sensing With Communication Signals: From Information Theory to Signal Processing. *arXiv preprint arXiv:2502.10819* (2025).

[32] Shengheng Liu, Hao Wang, Mengguan Pan, Peng Liu, Yahui Ma, and Yongming Huang. 2023. 5G NR monostatic positioning with array impairments: Data-and-model-driven framework and experiment results. In *Proceedings of the 3rd ACM MobiCom Workshop on Integrated Sensing and Communications Systems*. 1–6.

[33] Sohrab Madani, Suraj Jog, Jesus O Lacruz, Joerg Widmer, and Haitham Hassanieh. 2021. Practical null steering in millimeter wave networks. In *18th USENIX Symposium on Networked Systems Design and Implementation (NSDI 21)*. 903–921.

[34] Radosław Maksymiuk, Karol Abratkiewicz, Piotr Samczyński, and Marek Płotka. 2022. Rényi entropy-based adaptive integration method for 5g-based passive radar drone detection. *Remote Sensing* 14, 23 (2022), 6146.

[35] Matlab. 2025. *5G Toolbox*. https://www.mathworks.com/products/5g.html

[36] Naoual El-Djouher Mebtouche and Nadia Baha. 2023. Robust UAV detection based on saliency cues and magnified features on thermal images. *Multimedia Tools and Applications* 82, 13 (2023), 20039–20058.

[37] Nikhil K. Nataraja, Sudhanshu Sharma, Kamran Ali, Fan Bai, Rui Wang, and Andreas F. Molisch. 2025. Integrated Sensing and Communication (ISAC) for Vehicles: Bistatic Radar With 5G-NR Signals. *IEEE Transactions on Vehicular Technology* 74, 4 (2025), 6121–6137. doi:10.1109/TVT.2024.3514573

[38] National Instruments. 2025. *USRP-2954 Software Defined Radio (SDR) Product Page*. https://www.ni.com/zh-cn/shop/model/usrp-2954.html

[39] Jacopo Pegoraro, Jesus O Lacruz, Michele Rossi, and Joerg Widmer. 2024. HiSAC: high-resolution sensing with multiband communication signals. In *Proceedings of the 22nd ACM Conference on Embedded Networked Sensor Systems*. 549–563.

[40] Rui Peng, Yafei Tian, and Shengqian Han. 2024. Disturbance-Avoidant Wireless Gesture Recognition with 5G-NR Cellular Signal. In *2024 IEEE 35th International Symposium on Personal, Indoor and Mobile Radio Communications (PIMRC)*. 1–6. doi:10.1109/PIMRC59610.2024.10817233

[41] Rui Peng, Yafei Tian, and Shengqian Han. 2024. Enhanced Wireless Sensing by Exploiting Opportunistic 5G-NR Signals. In *2024 IEEE 99th Vehicular Technology Conference (VTC2024-Spring)*. IEEE, 01–07.

[42] Ahmed N Sayed, Hajar Abedi, Omar M Ramahi, and George Shaker. 2024. Enhanced UAV detection and classification using machine learning and MIMO radars. *IEEE Transactions on Microwave Theory and Techniques* (2024).

[43] Savio Sciancalepore, Omar Adel Ibrahim, Gabriele Oligeri, and Roberto Di Pietro. 2020. PiNcH: An effective, efficient, and robust solution to drone detection via network traffic analysis. *Computer Networks* 168 (2020), 107044.

[44] Yumeng Sun, Jinguang Li, Linwei Wang, Junjie Xv, and Yu Liu. 2024. Deep Learning-based drone acoustic event detection system for microphone arrays. *Multimedia Tools and Applications* 83, 16 (2024), 47865–47887.

[45] Yifei Sun, Chao Yu, Yan Luo, Tony Xiao Han, Haisheng Tan, Rui Wang, and Francis CM Lau. 2025. An Experimental Study of Passive UAV Tracking With Digital Arrays and Cellular Downlink Signals. *IEEE Open Journal of the Communications Society* (2025).

[46] Abigael Taylor and Dominique Poullin. 2025. UAV Detection Using 4G-LTE-Based Passive Radar. *IEEE Trans. Aerospace Electron. Systems* (2025).

[47] Erik Tegler, Max Modig, Per Skarin, Kalle Åström, Magnus Oskarsson, and Gabrielle Flood. 2025. Detection and Localization of Drones and UAVs Using Sound and Vision. In *Proceedings of the Computer Vision and Pattern Recognition Conference*. 6650–6658.

[48] Joel A Tropp and Anna C Gilbert. 2007. Signal recovery from random measurements via orthogonal matching pursuit. *IEEE Transactions on information theory* 53, 12 (2007), 4655–4666.

[49] Zhiqing Wei, Fengyun Li, Haotian Liu, Xu Chen, Huici Wu, Kaifeng Han, and Zhiyong Feng. 2024. Multiple Reference Signals Collaborative Sensing for Integrated Sensing and Communication System Towards 5G-A and 6G. *IEEE Transactions on Vehicular Technology* 73, 10 (2024), 15185–15199. doi:10.1109/TVT.2024.3410352

[50] Binbin Xie, Minhao Cui, Deepak Ganesan, Xiangru Chen, and Jie Xiong. 2023. Boosting the long range sensing potential of lora. In *Proceedings of the 21st Annual International Conference on Mobile Systems, Applications and Services*. 177–190.

[51] Shubo Yang, Yang Luo, Wang Miao, Changhao Ge, Wenjian Sun, and Chunbo Luo. 2021. RF signal-based UAV detection and mode classification: A joint feature engineering generator and multi-channel deep neural network approach. *Entropy* 23, 12 (2021), 1678.

[52] Jia Zhang, Xin Na, Rui Xi, Yimiao Sun, and Yuan He. 2023. mmHawkeye: Passive UAV detection with a COTS mmWave radar. In *2023 20th Annual IEEE International Conference on Sensing, Communication, and Networking (SECON)*. IEEE, 267–275.